Research Square

Preprints are preliminary reports that have not undergone peer review.
They should not be considered conclusive, used to inform clinical practice,
or referenced by the media as validated information.

Single-Shot Replica-Free Common-Path Quantitative Phase Imaging with Doubled Field of View

Piotr Zdańkowski

Piotr.Zdankowski@pw.edu.pl

Warsaw University of Technology https://orcid.org/0000-0003-3526-3233

Aleksandra Piekarska

Warsaw University of Technology

Mikolaj Rogalski

Warsaw University of Technology

Marzena Stefaniuk

Nencki Institute of Experimental Biology https://orcid.org/0000-0003-4725-8909

Maciej Trusiak

Warsaw University of Technology https://orcid.org/0000-0002-5907-0105

Article

Keywords: shearing interferometry, grating interferometry, common-path interferometry, quantitative phase imaging, phase retrieval, replica phase removal, digital holographic microscopy

Posted Date: September 7th, 2026

DOI: https://doi.org/10.21203/rs.3.rs-10652545/v1

License: This work is licensed under a Creative Commons Attribution 4.0 International License.
Read Full License

Additional Declarations: There is no conflict of interest

Single-Shot Replica-Free Common-Path Quantitative Phase Imaging with Doubled Field of View

Aleksandra Piekarska [1], Mikołaj Rogalski [1], Marzena Stefaniuk [2], Maciej Trusiak [1], Piotr Zdańkowski [1*]

[1] Institute of Micromechanics and Photonics, Warsaw University of Technology, Warsaw, 02-525, Poland

[2] Laboratory of Neurobiology, BRAINCITY, Nencki Institute of Experimental Biology of Polish Academy of Sciences, Warsaw, 02-093, Poland

[*]Correspondence: piotr.zdankowski@pw.edu.pl

Abstract:

Common-path digital holographic microscopy is widely recognized for its outstanding temporal stability and low-noise quantitative phase imaging. However, standard implementations are fundamentally limited by the spatial overlap between the object beam and its laterally shifted replica, which restricts high-fidelity imaging to sparse samples and wastes over half of the usable detector area. In this work, we break this paradigm by demonstrating a single-shot, replica-free common-path framework that doubles the effective field of view without any mechanical translation. By utilizing wavelength-dependent diffraction in polarization gratings, we shift wavefront shear control entirely into the spectral domain. This optical layout is powered by a novel Gradient Descent-based Replica Separation optimization algorithm, a powerful reconstruction engine that decouples overlapping fields without the rigid phase-sign constraints or low-frequency phase loss characteristic of analytical separation methods. By simultaneously illuminating the specimen with three discrete wavelengths and capturing a single multichannel color hologram, we retrieve the necessary shear states in a single camera frame. This enables complete, replica-free phase reconstructions of highly dynamic, dense specimens at camera-limited framerates. We validate our framework using quantitative phase targets and complex biological systems, showcasing high-fidelity reconstructions of fixed neural networks and demonstrating the real-time tracking of dense, moving yeast cell cultures where spatial replica overlap is unavoidable. Thanks to the integration of the environmental robustness of common-path geometry with high-speed, high-density spatial multiplexing, this technique introduces a versatile, high-throughput tool for advanced biomedical imaging.

Keywords: shearing interferometry, grating interferometry, common-path interferometry, quantitative phase imaging, phase retrieval, replica phase removal, digital holographic microscopy

Introduction

Quantitative phase imaging (QPI) is a label-free imaging method for the investigation of transparent cells and tissues[1]. By measuring the delay of light caused by the semi-transparent sample, QPI enables quantitative reconstruction of sample parameters such as the refractive index and dry mass[2]. This method is widely applied in the analysis of cell morphology[3] and the monitoring of physiological processes[4,5], which is of key importance for, e.g., evaluation of drug efficacy[6] and the development of new therapeutic strategies[7,8].

One of the most widely used QPI techniques is digital holographic microscopy (DHM), which achieves phase measurement by decoding the optical fringe patterns, that are produced via the interference of at least two optical beams. In its standard implementation, the interfering object and reference beams propagate along separate paths[2]. Although this configuration is well-established and widely used, it has certain limitations: large size and susceptibility to environmental disturbances, such as temperature fluctuations or mechanical vibrations. Additionally, due to substantial differences in optical path lengths across the entire field of view, maintaining consistently high contrast requires the use of highly coherent light sources. This, in turn, leads to undesirable phenomena such as speckle noise.

An alternative to classical reference beam DHM is a common-path configuration[9–16], in particular shearing interferometry[11,12], in which the object beam interferes with its spatially shifted copy. This ensures nearly identical optical paths, which eliminates the separate reference arm and simplifies the setup. Moreover, it

enables operation under reduced-coherence illumination, while maintaining high interferogram contrast. The lateral shift is implemented, among others, using shear plates, diffraction gratings[17–22], Wollaston prisms[23], or beam displacers[24,25].

Reconstruction-wise, common-path DHM systems can be divided into two groups, depending on the magnitude of the introduced shear. The first comprises gradient-based methods, in which the shear value is smaller than the lateral size of the measured objects - typically close to the spatial resolution of the system. In this configuration, the interferogram encodes the spatial derivative of the object phase. Therefore, recovering the full phase information requires recording the gradient components in two directions and an additional numerical integration procedure. To this end, stringent conditions must be satisfied: orthogonality of the shear vectors[17,26] and precise knowledge of their values[27] - identical for both vectors. Simple solutions employed for this purpose are susceptible to noise accumulation and error propagation[28–30], whereas advanced algorithms are time-consuming and often require multiple holograms[27]. The recently proposed optimization-based OSI-flex approach relaxes the requirement of orthogonality of the shear vectors and precise knowledge of their values. However, it still requires a good initial estimate of these parameters, is more computationally expensive than solutions that impose these requirements, and requires hyperparameter fine-tuning[31].

The second group of methods are the total shear configurations[13,23,24,32–34], in which the lateral displacement between interfering beams is larger than the lateral dimensions of measured objects. For this configuration it is extremely important that measured area is either only sparsely covered with the measured objects, or it contains a large object-free area. Otherwise, images from different regions of the sample will overlap on the detector with the laterally shifted replica, causing mutual signal annihilation and preventing the imaging of dense samples. For this reason, samples for which the size of the required reference region may be insufficient cannot be correctly imaged using this method.

To extend the applicability of total shear methods to dense and extended samples, there were proposed methods that rely on modifying one of the interfering beams to remove object information[14,16]. Although they enable imaging of dense and complex objects, they result in increased optical system complexity[35] and a significant reduction of the effective field of view, often by more than half[19–21]. In turn, the use of low-pass filtering by means of a pinhole for this purpose renders the system difficult to precisely align and sensitive to mechanical instabilities[14,16,36,37].

Another solution for imaging complex samples is to employ shear scanning to separate overlapping fields. These include, among others, Cepstrum-based interference microscopy (CIM)[38–40] and R2D-QPI (replica-removed doubled-FOV QPI)[41]. The CIM approach relies on highly precise orthogonal single-pixel shears for temporal scanning, and the high-pass filtering, which increases system complexity and might suppress low-frequency phase components. On the contrary, the R2D-QPI approach, recently proposed by our group, constitutes a general methodology that enables separation of overlapping phase information from a set of at least 2 phase images with arbitrarily chosen shears via the proposed multi-shear replica removal (MRR) algorithm. This methodology can be implemented in various total shear hardware configurations, provided they can generate interference patterns with variable shear values.

The current implementation of R2D-QPI method was based on polarization grating total shear configuration, where the variable shear was achieved via axial scanning of one of the gratings. However, this introduced significant limitations to the system: mechanical wear, vibrations, and limited acquisition speed. The requirement to record a sequence of frames precludes the possibility of imaging dynamic samples.

In this work, we propose a novel replica removal method based on the wavelength-scanning regime. In the proposed approach, controlled variation of the replica separation is achieved by changing the illumination wavelength, without requiring any mechanical movement. The proposed hardware modification is accompanied by a bespoke reconstruction procedure: (i) we introduce a new preprocessing stage that compensates for objective chromatic aberration, and (ii) we propose a novel gradient descent-based

replica separation (GDRS) algorithm, which achieves significantly more robust reconstruction than the original MRR method without requiring any a priori information about the sample's phase sign.

The proposed method was validated using quantitative phase targets and live cell samples, consistently achieving reliable separation of the fields of view of both replicas (doubling the effective spatial coverage of the sample). The complete elimination of mechanical scanning enables fast and robust phase imaging while preserving the simplicity and high quality (high SNR) of low coherence common-path interferometer.

Results

2.1 Experimental Setup and Reconstruction Strategy

The common-path configuration described in this article - Fig. 1(a) - is based on the use of the polarization grating (PG) module, shown in Fig. 1(b)[13,31,34,41], built from two identical polarization gratings arranged in series. It splits the illuminating beam into two diffraction orders (±1) with orthogonal circular polarizations and generates a lateral wavefront shear τ_λ.

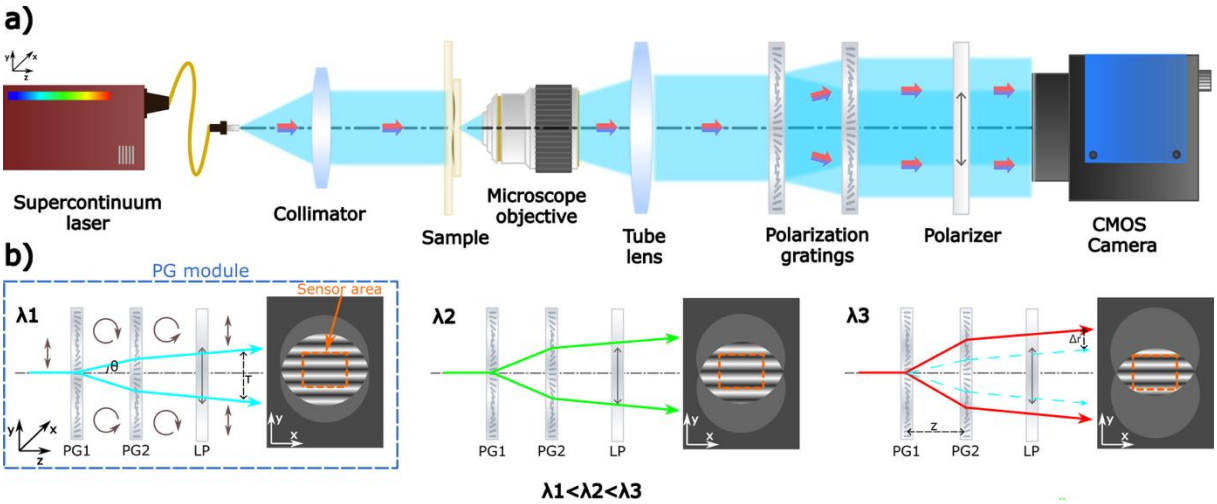


Fig. 1 | (a) Optical setup of a common-path holographic microscopy system based on polarization gratings for single-shot imaging. (b) Schematic of beam propagation through the grating module depending on the illumination wavelength λ. PG – polarization grating, LP – linear polarizer, λ – illumination wavelength, τ – shear between the beams, θ – diffraction angle, z – distance between the gratings, $\Delta\mathbf{r}$ – beam displacement between frames. In the schematic marked with the blue frame, successive polarization states of the beam are schematically illustrated using brown arrows. For clarity, these markings are omitted in the remaining schematics; however, they apply to all cases.

Rotation of one grating around the optical axis changes the deflection angle of the beams, allowing simple adjustment of the interferogram carrier frequency. In the measurements, we set the gratings' mutual rotation to obtain an optimal carrier frequency for the phase reconstruction using the Fourier transform method (FTM).The value of the shear τ_λ depends on the diffraction angle θ_λ and on the distance z between the gratings[34,41] (Fig. 1(b)). Variants of interferogram parameter modulation, i.e., translation and rotation of the gratings, are described in detail in the Methods section. When the shear value τ exceeds the camera sensor diagonal, the registered overlapping phase image will contain information from two disjoint areas of the object, effectively doubling the field of view. In order to recover undisturbed phase information from overlapped object replicas, it is necessary to record a series of at least $N = 2$ interferograms for different shear values τ.

In this work, we present a new method for controlling the shear value τ_λ based on modifying the diffraction angle θ_λ, in contrast to our previously reported R2D-QPI implementation, in which the shear variation was realized mechanically by physically translating one of the diffraction gratings. Replacing the mechanical scan with wavelength scanning eliminates all moving parts from the shear-control path, making the shear adjustment faster, fully repeatable and free from mechanical misalignment. The diffraction angle depends,

among other factors, on the wavelength of the incident light λ, via the diffraction grating equation $\theta_\lambda = \sin^{-1}(\lambda/d)$, where d is the grating period. The larger the wavelength λ, the larger the angle θ_λ and, consequently, the greater the shear τ. Modulation of the shear value τ_λ, by changing the wavelength λ, is implemented in two modes, as shown in Fig. 2:

1. Wavelength scanning mode (Fig. 2(a)): Sequential illumination with different λ (step, e.g., $\Delta\lambda = 5\ nm$) and recording of the interferogram with a monochromatic camera for each λ.

2. Single-shot mode (Fig. 2(b)): Illumination with three discrete λ (i.e., $\lambda_1 = 458\ nm$, $\lambda_2 = 550\ nm$, $\lambda_2 = 615\ nm$) simultaneously. A single interferogram is recorded with a color (RGB) camera and then separated into the individual color channels.

These wavelengths were selected experimentally to limit the spectral crosstalk. It is important to emphasize that replacing grating scanning[41] with wavelength scanning is not merely a trivial modification for obtaining a variable shear (τ) in a faster and more robust manner. Beyond this, it additionally enables high-speed imaging with single-shot acquisition and wavelength-based speckle-noise suppression, capabilities that cannot be achieved in the grating-scanning approach. However, it also requires accounting for chromatic aberrations (transverse and longitudinal) and necessitates additional processing steps.

Different wavelengths focus at slightly different planes (longitudinal chromatic aberration), introducing varying defocus between the recorded frames. Therefore, the reconstruction process begins with phase reconstruction using Fourier transform method for each frame in the series. The optical field recovered in this way is numerically refocused using the angular spectrum method[42]. A change in wavelength also leads to a change in the system magnification (transverse chromatic aberration), resulting in a different mapping of the sizes of the same structures. This effect is corrected by applying geometric operations, consisting of image scaling using bicubic interpolation (see methods section for detailed description). Subsequently, the phase value $\varphi_{\pm 1}$ recovered from each frame is scaled with respect to its corresponding wavelength. This scaling reflects the dependence of the phase shift on the wavenumber ($k = 2\pi/\lambda$) and represents a novel element introduced in the GDRS method (Fig. 2). At the same time, the value of the phase shift $\Delta\varphi$ also depends on the difference in refractive indices ($n_{probe} - n_{reference}$). The refractive index of a medium is a dispersive function, and its variations as a function of wavelength are related to absorption of illumination, which is formally described by the Kramers–Kronig relations[43]. The investigated biological objects are mainly composed of water, which is characterized by minimal absorption in the visible range. Consequently, the change in the refractive index difference within the illumination range used in our experiment, as well as its influence on the variation of the phase shift value, are negligibly small[44,45]. After refocusing and correcting the chromatic aberrations, the resulting dataset, together with the estimated values of $\Delta\mathbf{r}$ (the difference in τ between frames) is then processed using the novel GDRS algorithm, which is described in detail in the Supplementary Information (Supplementary Note 1).

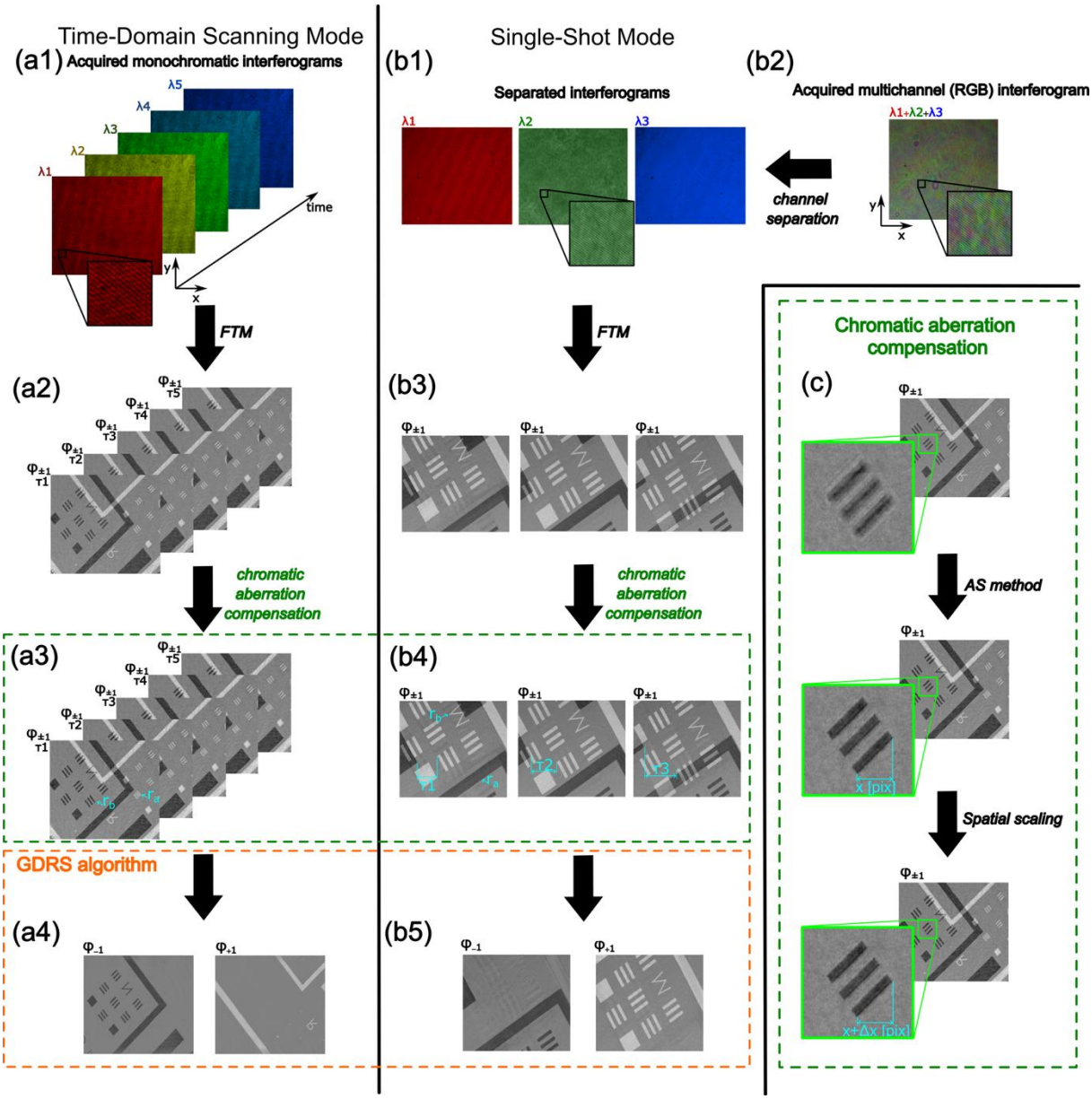


Fig. 2 | Data-processing workflow of the GDRS algorithm for different measurement scenarios. (a) Processing of data acquired in the wavelength-scanning mode. (b) Processing of data acquired in the single-shot mode under triple-wavelength illumination. Panels (a1), (b2) show the recorded interferograms with a zoomed-in view of the interference pattern. For the single-shot mode, (b1) presents the set of interferometric images obtained by separating the color channels of the recorded frame. The next step involves reconstructing optical field using FTM: (a2), (b3) display the phase information that can be recovered from this field. Sections (a3), (b4) present the phase information $\varphi \pm 1$ with visible replica overlap after correction of focus and magnification (see panel c), where r_a and r_b indicate the phase encoded in the ±1 orders, and τ represents the lateral spatial shift between the interfering beams. Finally, (a4), (b5) show the separated phase reconstructions for both diffraction orders FOVs, obtained from a set of reconstructions corresponding to different values of the shift τ_λ.

2.2 Experimental results

2.2.1 Comparison between R2D-QPI and GDRS

To compare the impact of the replica shift variation method on imaging quality, we collected two datasets, each consisting of $N = 20$ interferograms recorded at different, yet mutually comparable, shear values – one dataset obtained via grating scanning and the other via wavelength scanning.

The phase target (Lyncee Tec, Borofloat 33 glass with etched structures of 125 nm height) was imaged using a 5x/0.12 microscope objective lens and a supercontinuum light source. Both measurement series were reconstructed using the GDRS algorithm, such that the only factor differentiating them was the shear-scanning method. In the first series depicted in Figures 3(a1)-(a4), serving as a reference, an R2D-QPI[41] approach was applied. The change in the shear value τ was obtained by translating the diffraction grating (PG2) along the optical axis, with a step of $\delta = 0.5$ mm, at a constant illumination wavelength $\lambda = 535$ nm. In the second series (Figures 3(b1)-(c3)), the proposed new method was employed, in which the change in the shear value τ_λ was achieved by varying the illumination wavelength λ over the range from 490 nm to 585 nm with a spectral step of $\Delta\lambda = 5$ nm. The adopted experimental parameters were selected to ensure a fair comparison between methods. Both series were acquired with the same interferogram carrier frequency and a matched shear value τ, ensuring a comparable object–replica overlap in each case. The grating translation step in Series 1 and the spectral step in Series 2 generated a similar intra-replica shift value $\Delta\mathbf{r}$, corresponding to $|\Delta\mathbf{r}| \approx 14$ pixels.

Figures 3(a1) and 3(b1) present the initial phase maps obtained using the Fourier transform method. The recovered phase $\varphi_{\pm 1}$ corresponds to the phase difference $\varphi_{+1} - \varphi_{-1}$ between two conjugated object replicas. In the case of wavelength scanning, an additional processing step is required to compensate for defocus resulting from chromatic aberration. The focus was adjusted for the central frame of the sequence (Fig. 3(c1)), causing the frames at the spectral extremes, such as the first frame (Fig. 3(c2)), to be defocused. Therefore, the ASM algorithm was applied prior to reconstruction, and the result of the defocus correction is shown in Figure 3(c3). We performed the reconstruction of the separated phase distributions φ_{+1} and φ_{-1} (corresponding to the +1 and -1 diffraction orders) for the entire series ($N = 20$). Figures 3(a2), (a3), (b2), and (b3) present the results for both fields of view, covering the “N” and “R” groups, respectively. The reconstructions obtained for both series are free from visible replica artifacts, which directly confirms that the proposed method enables achieving similar imaging capabilities as the original R2D-QPI approach.

To examine the influence of overlapping object replicas on the correctness of the phase reconstruction, the mean phase value and its standard deviation were calculated in two characteristic regions. In the first region fragments of the object overlap (Fig. 3, blue square no. 2) and the phase information degrades due to the destructive superposition. The second is an area without overlap (Fig. 3, blue square no. 1), adopted as a reference point for the correct phase representation. As indicated by the results summarized in Table 1, in both measurement scenarios, the GDRS algorithm enabled correct reconstruction of the phase value in the region with overlapping object replicas, despite the inherent loss of information occurring there.

Table 1 Average phase values along with their standard deviation for the areas marked with a blue rectangle in Fig. 3.

	Phase$\varphi_{\pm 1}$ in Region 1 [rad]	Phase $\varphi_{\pm 1}$ in Region 2 [rad]	Phase φ_{-1} in Region 1 [rad]	Phase φ_{-1} in Region 2 [rad]
Grating position scanning mode	-0.58 ± 0,04	0.11 ± 0,08	-0.62 ± 0,03	-0.60 ± 0,04
Wavelength scanning mode	-0.62 ± 0,05	0.07 ± 0,08	-0.64 ± 0,02	-0.64 ± 0,03

The key differences in the quality between the modes become apparent during the analysis of the phase profile, marked with an orange line passing through one of the elements of the test structure in the reconstruction (Figs. 3(a3), (b3)). The cross-sections shown in Figs. 3(a4) and (b4), as well as the standard deviation (STD) of the phase values in object-free regions, clearly indicate that the reconstruction from Series 2 exhibits a much more homogeneous background. This occurs because the speckle pattern causing this inhomogeneity is wavelength-dependent, so during processing, such objects that do not repeat in each frame are averaged out by the algorithm.

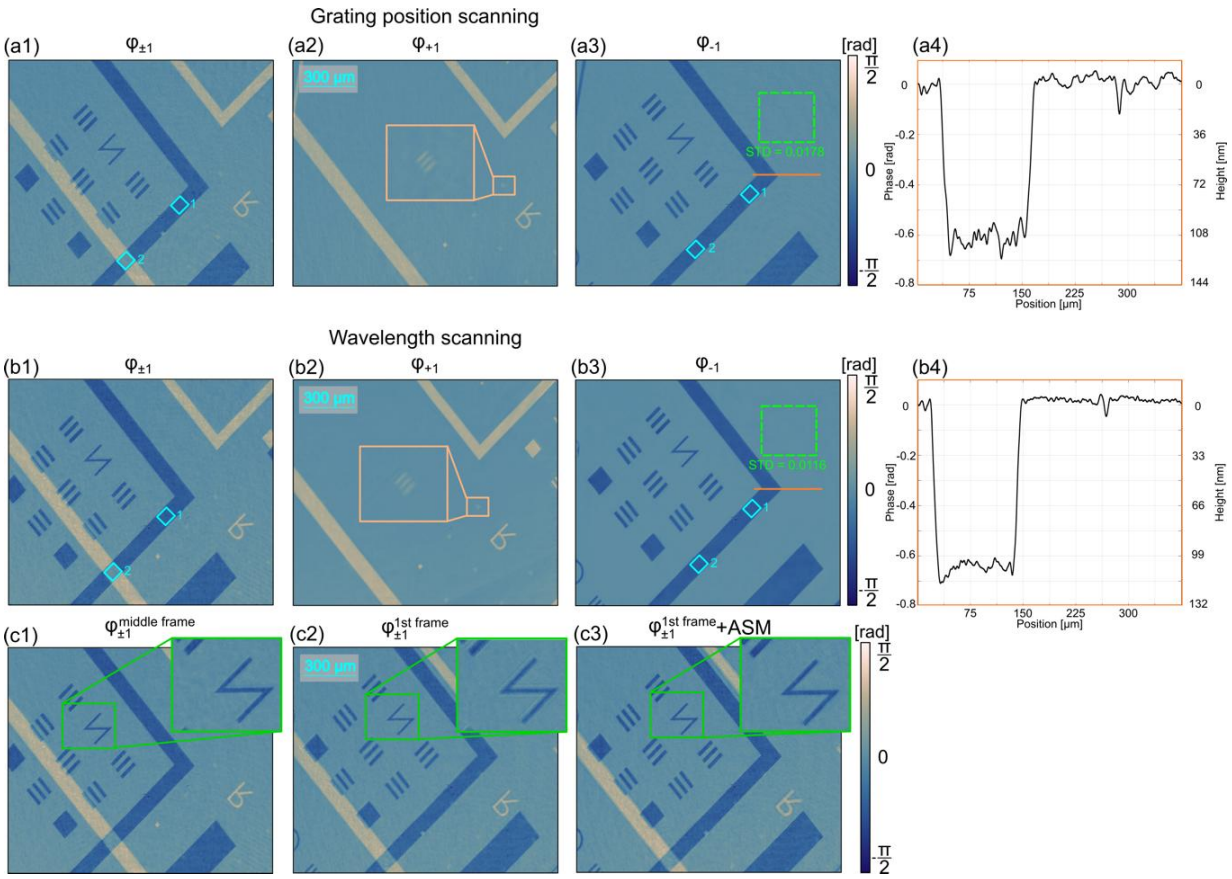


Fig. 3 | Comparison of phase-imaging results obtained for a phase resolution target using grid-shift scanning and wavelength-scanning approaches. (a) Imaging results for varying replica displacement introduced by translation of the grating. (b) Imaging results for varying replica displacement achieved through change of the illumination wavelength (c) Defocus correction results. (a1), (b1), (c) Phase reconstructions $\varphi_{\pm 1}$ obtained using FTM. (a2)-(a3), (b2)-(b3) Reconstructed φ_{+1} and φ_{-1} phase distributions, with the orange line indicating the cross-section shown in (a4) and (b4).

2.2.2 Parameter analysis in GDRS

Within the experimental studies, the performance of the GDRS algorithm was investigated for different values of key parameters – spectral step $\Delta\lambda$, number of frames N, and the total spectral range $(N-1)\cdot\Delta\lambda$. A comparison of the performance of the MRR and GDRS algorithms is presented in Figure 4. Figures 4(a1)–(e1) show the phase map recovered from a single frame $\varphi_{\pm 1}$, while columns 4(a2)–(e2) and 4(a3)–(e3) contain the reconstructed phase images $\varphi_{-1}$for a single field of view obtained using the MRR and GDRS algorithms, respectively. Column (a4)–(e4) shows phase profiles along a cross-section passing through the elements of the test structure. The first investigated parameter affecting the reconstruction quality is the number of recorded frames N. The performance of both algorithms was evaluated for their minimum number of required frames, $N = 2$. For this purpose, a measurement series was acquired by illuminating the sample with wavelengths of $\lambda = 530$ and $\lambda = 535$ nm, and the reconstruction results are shown in Figure 4(a). In the case of the MRR algorithm, the small number of frames causes difficulties in reproducing the low-frequency components (Figure 4(a2)); this issue was investigated in detail in our previous work[41]. In contrast, the GDRS algorithm successfully reconstructed the phase even with such a limited dataset (Fig. 4(a3)).

Another important parameter is the spectral step $\Delta\lambda$, which directly determines the magnitude of the beam shift $\Delta\mathbf{r}$ between frames. To illustrate its influence, two measurement series were performed - one with a very small value of $\Delta\lambda = 5$ nm (Figure 4(b)) and another with a very large value of $\Delta\lambda = 160$ nm (Figure 4(c)). In each series, two wavelengths were selected symmetrically with respect to the central wavelength of

$\lambda = 545$ nm. It was observed that for such extreme values of the spectral step $\Delta\mathbf{r}$, the MRR algorithm encounters difficulties in faithfully recovering the phase from a single field of view. An excessively large step leads to a situation in which substantial parts of the object are visible only in a single frame, resulting in artifacts in the reconstructed phase (Figure 4(c2)). Conversely, an excessively small spectral step limits the ability to correctly reproduce the low-frequency components (Figure 4(b2)). In this case, only the edges oriented perpendicular to the shift direction $\Delta\mathbf{r}$ are reconstructed correctly. The GDRS algorithm is robust against these limitations, and both reconstructions exhibit good quality (Figures 4(b3) and 4(c3)).

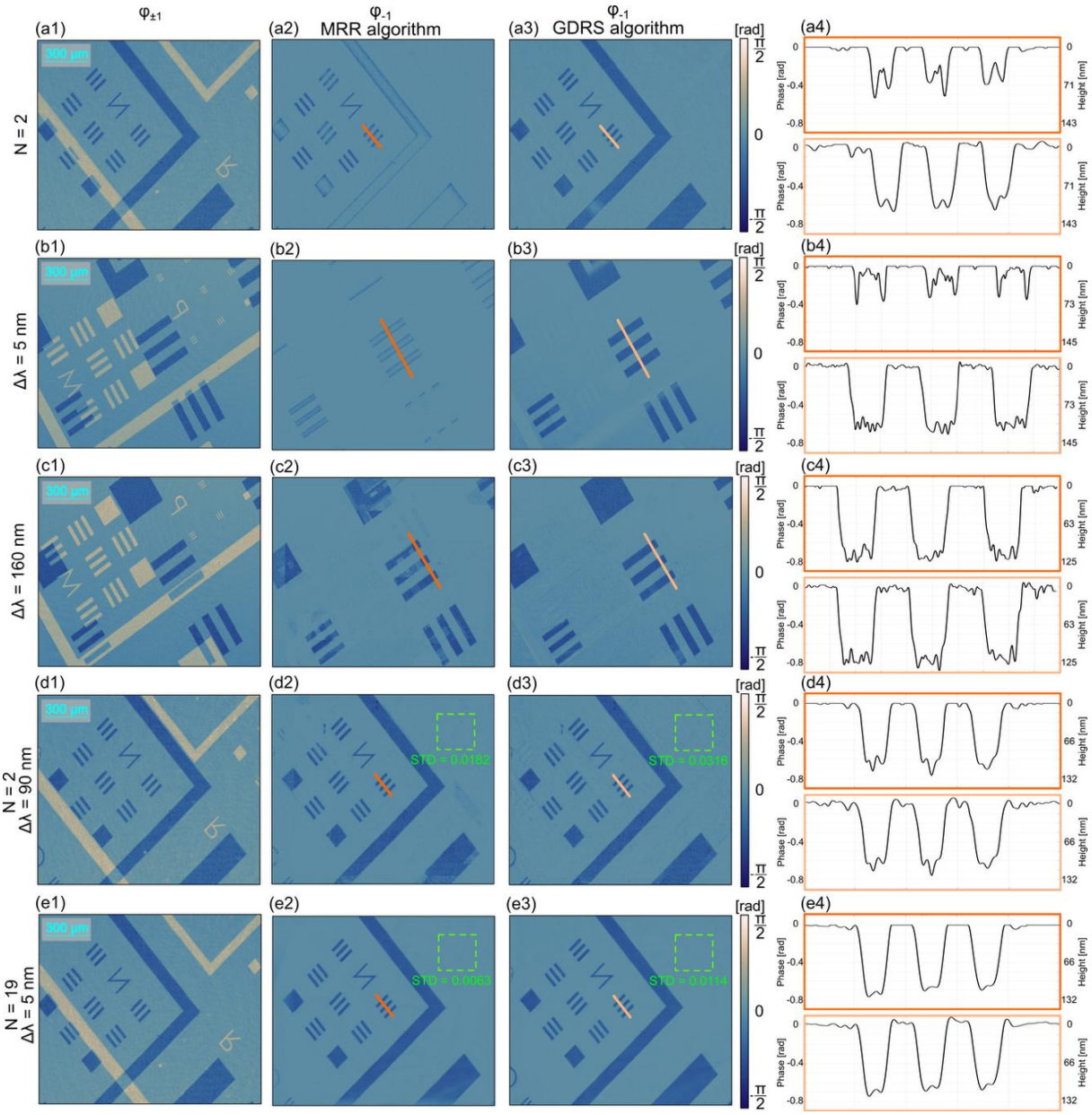


Fig. 4 | Comparison of reconstruction results obtained for different values of key imaging parameters. The phase reconstructions $\varphi_{\pm 1}$ with visible replica overlap and the corresponding phase distributions φ_{-1} obtained using the MRR and GDRS algorithms are shown for: (a) a small number of frames ($N = 2$), (b) a small spectral step ($\Delta\lambda = 5$ nm), (c) a large spectral step ($\Delta\lambda = 160$ nm), and a constant total beam shift: (d) $N = 2, \Delta\lambda = 90$ nm, (e) $N = 19, \Delta\lambda = 5$ nm.

It should be emphasized that the key factor determining the quality of the reconstructed phase is the value of the product $(N-1)\cdot\Delta\mathbf{r}$, defined as the total beam shift, rather than the individual components of this parameter. This relationship was confirmed using two measurement series with a constant total shift but different spectral sampling: $\Delta\lambda = 90$ nm, $N = 2$ (Figure 4(d)) and $\Delta\lambda = 5\,nm,\ N = 19$ (Figure 4(e)). The

obtained phase reconstructions φ_{-1} demonstrate that, despite the decreasing spectral step $\Delta\lambda$ accompanied by an increasing number of frames N, the quality of low spatial frequency reproduction remains unchanged even for the MRR algorithm. This is precisely due to the constant value of the product $(N-1)\cdot\Delta\mathbf{r}$. For a smaller number of frames and a large spectral step (Figure 4(d)), the reconstruction obtained with the MRR algorithm contains artifacts caused by substantial parts of the object being visible only in a single frame, similarly to the case shown in Figure 4(c2). The GDRS algorithm is considerably less sensitive to this effect (Figure 4(d3)). The STD value in the background region of the phase reconstruction was calculated for both algorithms. The lower STD obtained for the MRR algorithm results from the phase sign constraint imposed in MRR. This constraint enforces exclusively negative/positive or zero values in the background, whereas GDRS allows unrestricted background fluctuations around zero. A comparison of the results obtained for both datasets (Figures 4(d) and 4(e)) indicates that increasing the number of recorded frames N provides an additional benefit in the form of noise averaging, thereby improving the signal-to-noise ratio in the final reconstruction.

Considering all presented results – including the tests of the influence of the number of frames N, spectral step $\Delta\lambda$, and total beam shift $(N-1)\cdot\Delta\mathbf{r}$, it can be concluded that the GDRS algorithm is significantly more robust to extreme values of the key parameters. Consequently, the selection of their ranges is not as critical for reconstruction quality as in the case of the MRR algorithm. It should be noted that we intentionally focused on boundary cases in order to highlight the differences between the algorithms. This may, however, give the impression that the selection of imaging parameters requires particular precision. In practice, highly comparable results are obtained over a broad range of parameter values. This is confirmed by the root mean square error (RMSE) of the reconstructed phase, shown in Figure 5, calculated with respect to the reference phase map (ground truth).

In the first scenario, with a fixed spectral step of $\Delta\lambda = 5$ nm between consecutive frames (Fig. 5(a)), it can be observed that increasing the number of frames beyond a certain point no longer significantly improves the reconstruction quality. Moreover, as the number of frames decreases, the GDRS algorithm reconstructs the phase substantially more accurately than the MRR algorithm. The reconstruction obtained from $N = 20$ frames was adopted as the ground truth. For the remaining cases ($N = 2, 3, 5, 10, and\ 15$), the illumination wavelengths were selected symmetrically with respect to the central wavelength of 535 nm.

A similar trend is observed in the second scenario, in which the total spectral shift was kept constant at $(N-1)\cdot\Delta\mathbf{r} = 90$ nm (Figure 5(b)). Although a larger number of frames results in lower reconstruction errors, the RMSE remains below 0.05 rad even for $N = 2$, provided that a sufficiently large total spectral shift is maintained. Interestingly, according to this metric, the GDRS algorithm exhibits slightly higher RMSE values than the MRR method. This is due to the reduced phase averaging in the background. In this case, the reconstruction obtained from $N = 19$ frames with $\Delta\lambda = 5$ nm was used as the ground truth. The remaining measurement series were acquired with the same total shift but different spectral sampling: $\Delta\lambda = 90\ nm, 45\ nm, 30\ nm, 10\ nm, and\ 5\ nm$.

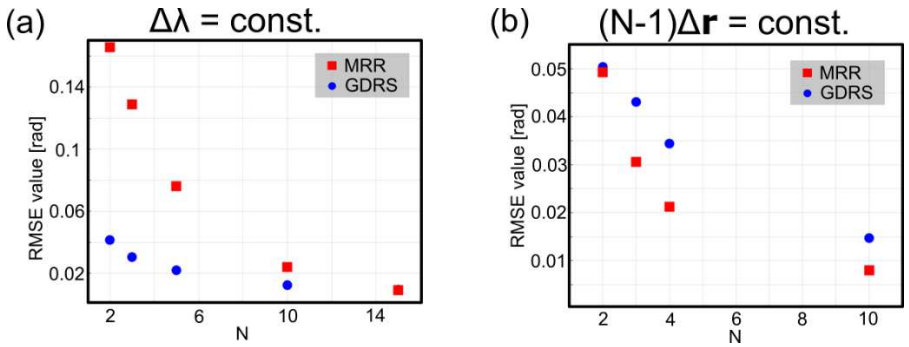


Fig. 5 | Root mean square error of the reconstructed phase as a function of the number of frames used for reconstruction, for a fixed (a) spectral step $\Delta\lambda$ and (b) total shift $(N-1)\cdot\Delta r$.

2.2.3 Single-shot imaging

Next, we evaluated the method capabilities to remove the object replica using a single shot acquisition with color camera. Figure 6 shows the phase reconstructions $\varphi \pm 1$ (Figure 6(a)) together with the corresponding phase distributions (φ_{+1} and φ_{-1}) for the ±1 diffraction orders (Figure 6(c), (d)). Figure 6(e) shows the superposition of the reconstructed phase maps φ_{+1} and φ_{-1}, while the cross-sectional profiles extracted along the orange line (Fig. 6(b), (f)) demonstrate the agreement between the reconstructed phase distributions and the original data. The same cross-section, taken at an identical location on the object for a single field of view, is marked by the dashed orange line. The measurement was performed by acquiring a single frame using a 10×/0.25 microscope objective, with the sample illuminated by a beam composed of three wavelengths: 458 nm, 550 nm, and 615 nm. Comparing the results obtained in single-shot mode with scanning-mode reconstructions with similar parameters, i.e. a small number of frames and a large spectral step (Fig. 4(c3)), we find that this method of acquiring a series of holograms only slightly degrades the reconstruction quality.

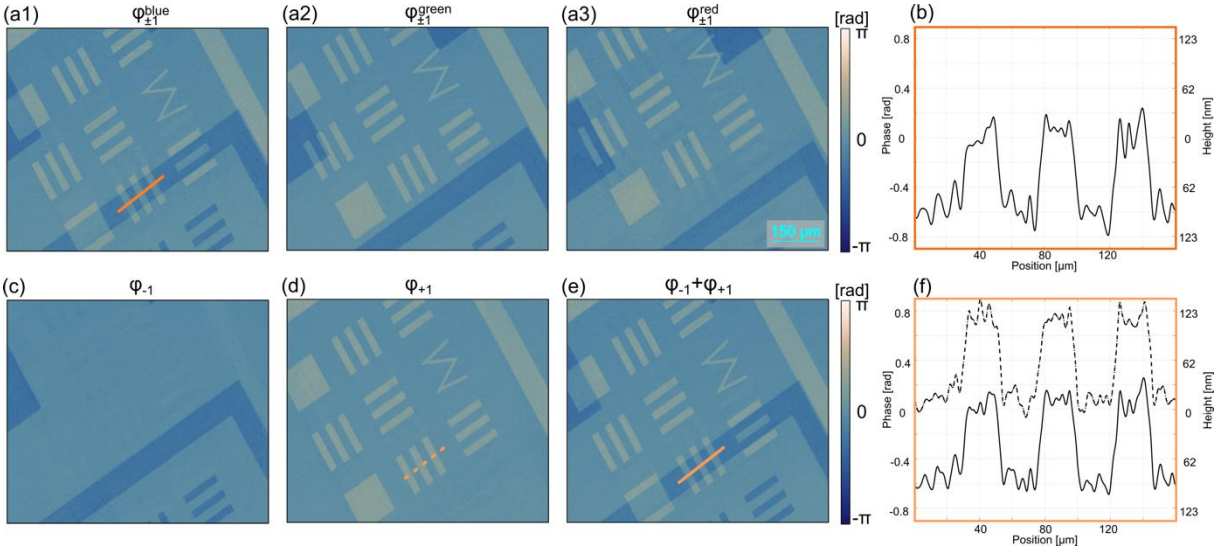


Fig. 6 | Single-shot phase imaging results for a phase resolution target. (a) Phase reconstructions $\varphi_{\pm 1}$ retrieved using the FTM, (c), (d) Separated phase maps (φ_{+1} and φ_{-1}), (e) Phase distribution after superposition of the two phase maps φ_{+1}+φ_{-1}, (b), (f) the cross-sections marked with the orange lines.

In the single-shot mode, a biological sample in the form of a fixed neuronal cell culture was also imaged under the same imaging conditions. The corresponding phase reconstruction results are presented in Figure 7(a1)–(c1). Both the axons themselves and the small cells in the background, which only weakly modulate the phase, were correctly reconstructed. The same object was imaged using the wavelength scanning method, recording N = 20 frames over a similar spectral range of 470–622 nm (step Δλ = 8 nm). The resulting phase reconstructions are shown in Figure 7(a2)–(c2). Most details and fine structures are visible in the reconstructions from both measurement modes. However, it should be emphasized that the wavelength scanning mode, due to the possibility of freely shaping the measurement parameters – including the key number of frames – enables obtaining a significantly better reconstruction quality for the investigated objects.

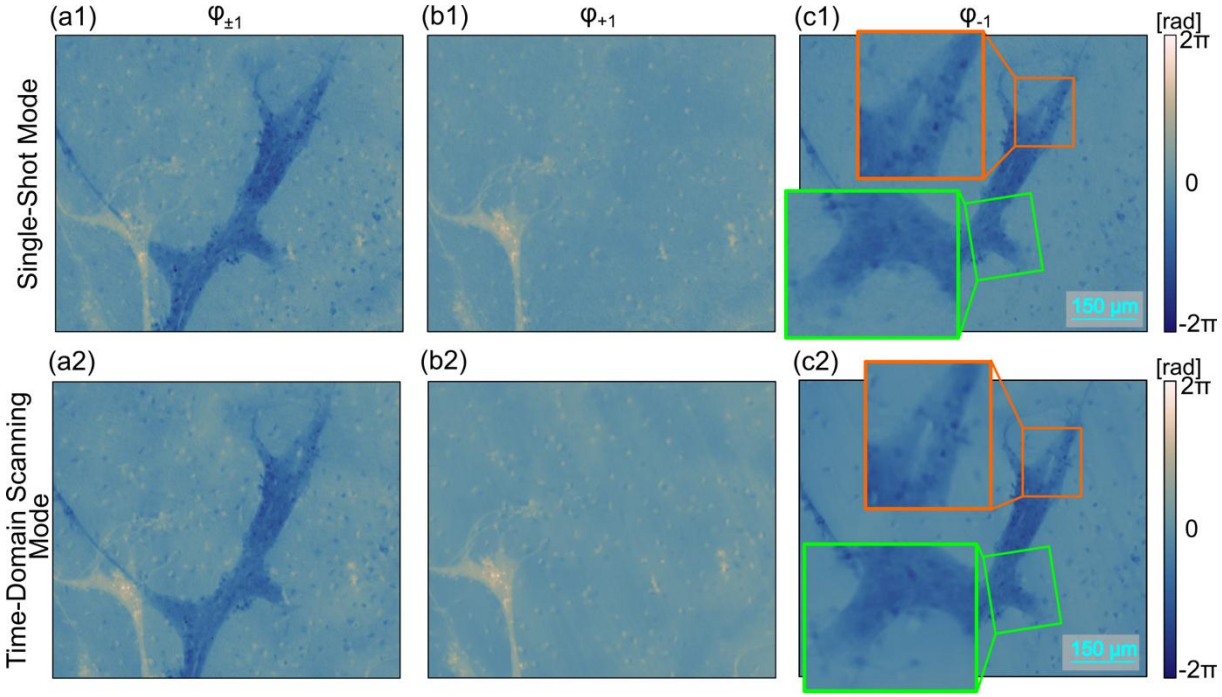


Fig. 7 | Single-shot phase imaging results compared to time-domain scanning mode results for a biological sample (neuronal cell culture). Phase reconstructions $\varphi_{\pm 1}$ retrieved using the FTM (for $\lambda = 458\ nm$ in single-shot mode and $\lambda = 518$ nm in scanning mode), together with the corresponding phase distributions (φ_{+1} and φ_{-1}). Measurements were performed in single-shot mode using illumination wavelengths of 458 nm, 550 nm and 615 nm in (a1)–(c1), and in time-domain scanning mode across a wavelength range of 470–622 nm in (a2)–(c2).

Despite the lower value of the space–bandwidth product (SBP) compared with the wavelength scanning method - a consequence of the Bayer filter, where pixel groups record only one-half or one-quarter of the sensor's native resolution - the single-shot mode enables the obtaining of results of comparable quality. Moreover, a significant advantage of this image acquisition method remains in its substantially higher temporal resolution, allowing for the observation of dynamic objects. To demonstrate this unique capability (for the first time in low coherence shearing DHM), we examined a sample containing moving yeast cells (Figure 8). Owing to the high cell density, finding a field of view in which the object did not overlap with its replica was practically impossible. The sample was illuminated simultaneously with three wavelengths – 458 nm, 550 nm and 615 nm, and imaged using a 40×/0.65 microscope objective.

Figure 8(a) shows the phase reconstruction with the fields of view from both beams superimposed. In the magnified regions marked in green and orange, it is evident that the high density of the sample leads to local replica overlap in the phase reconstruction. Nevertheless, as shown by the separated phase reconstructions φ_{+1} and φ_{-1} (Figs. 8(b) and 8(c)), the algorithm readily recovers both fields of view without loss of information or the introduction of additional artifacts. The inhomogeneous phase background corresponds to the true physical structure of the sample. Figure 8(c) shows the first recorded frame ($t = 0$ s), whereas Figures 8(d) and 8(e) present the 16th ($t = 11.2$ s) and 36th ($t = 25.2$ s) frames of the recorded sequence, respectively (frames acquired every 0.7 s). The remaining frames documenting the motion of the observed yeast cells are provided in the Supplementary Information. The occasional blinking artifacts visible in the frames are not reconstruction artifacts caused by limitations of the GDRS algorithm, but rather result from phase unwrapping errors.

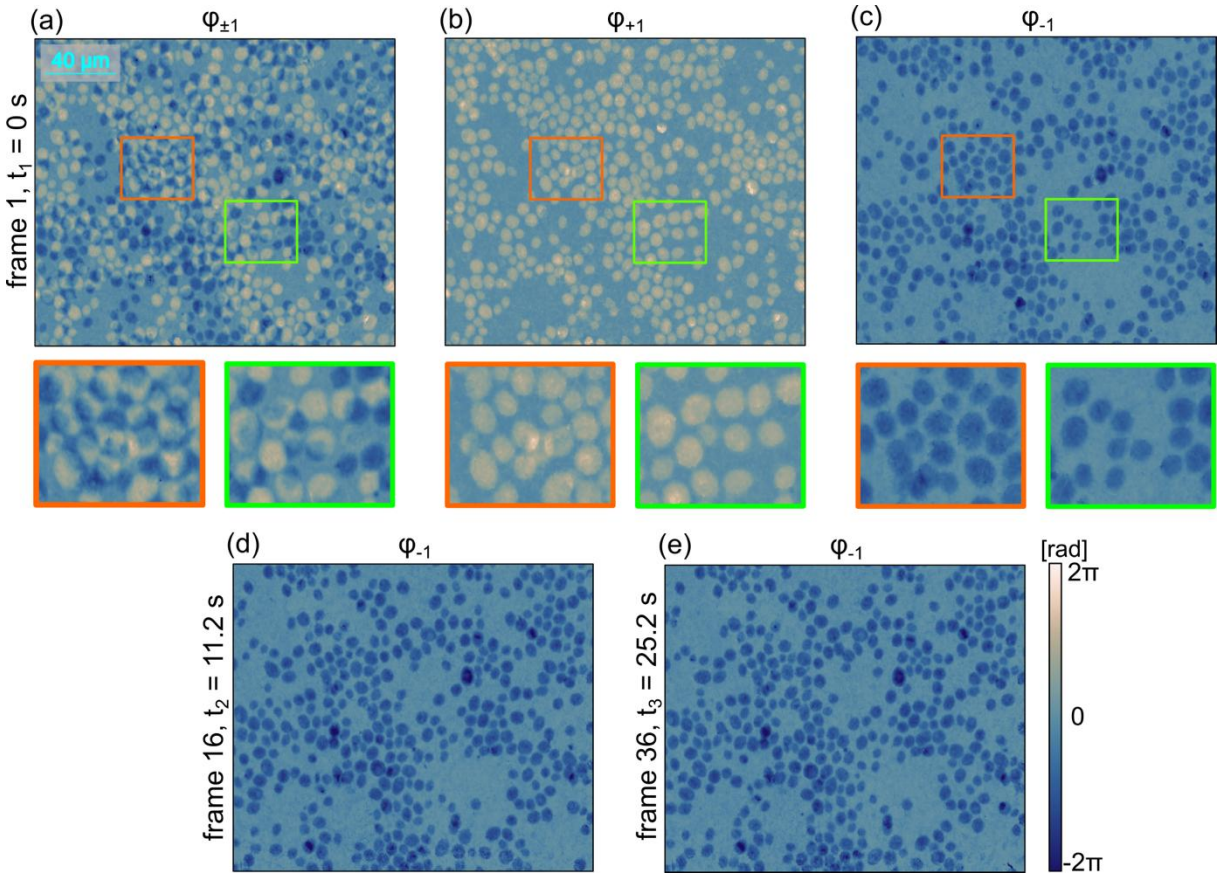


Fig. 8 | Single-shot phase-imaging results of a dynamic object (yeast cells). (a) Phase reconstructions $\varphi_{\pm 1}$ retrieved using the FTM (for $\lambda = 550\ nm$). (b-e) Corresponding phase distributions (φ_{+1} and φ_{-1}) for the ±1 diffraction order fields of view: (b,c) first frame in the recorded sequence, (d) 16th frame, and (e) 36th frame.

Discussion

In this work, we introduced wavelength-scanning multi-shear gradient descent-based replica separation – a method that removes one of the most fundamental constraints of common-path digital holographic microscopy: the loss of usable field of view caused by the overlap of the object and its replica. Rather than merely retrieving the phase, the GDRS algorithm exploits a series of holograms recorded at different shear values between the interfering beams to unambiguously decouple the object information from its replicas. As a result, the full camera sensor area becomes usable, effectively doubling the accessible field of view without sacrificing the inherent stability and simplicity of the common-path architecture.

The proposed framework enables replica-free QPI from a single acquisition, and thus the imaging of dynamic processes, thanks to shear control that is purely wavelength-based and entirely free of mechanical scanning. By eliminating the moving parts required by earlier implementations[38–41], the new approach simplifies the system architecture, improving the stability and repeatability of measurements, and enabling more effective noise averaging. Wavelength tuning does, however, introduce chromatic aberrations, and dedicated hologram processing stages were therefore developed to suppress their influence on the reconstructed phase. In parallel, the core of the reconstruction algorithm was modified and is now formulated as an optimization problem. Furthermore, unlike the MRR algorithm, the proposed approach does not impose a constraint on the phase sign and provides more robust reconstruction without requiring a priori knowledge of the sample phase sign. The new algorithmic structure enables improved recovery of low-frequency phase components, reduces artifacts at the edges of the field of view arising from the small number of frames, and decreases the sensitivity of reconstruction quality to the selection of measurement parameters. Moreover, unlike the CIM method, which uses high-pass filtering[38–40], this technique does not require such an operation.

It is worth noting that, due to the acquisition of a single frame using an RGB camera, the single-shot approach is associated with a reduction in effective spatial resolution. In a Bayer filter, the green channel records information from 50% of the pixels, whereas the red and blue channels record information from only 25%, corresponding to a twofold and fourfold reduction, respectively, in the number of sampling points compared with a monochrome sensor. This has a direct impact on the space–bandwidth product (SBP) in the single-shot configuration. Nevertheless, the numerical aperture of the objective lens remains the primary limiting factor. Modern sensors, both monochrome and RGB, provide a sufficient number of pixels to fully exploit the spatial frequency bandwidth transmitted by the optics; therefore, it is the objective lens, rather than the sensor, that constitutes the critical limiting factor.

Another factor limiting this approach is the color leakage problem. However, with an optimal selection of the illumination wavelengths matched to the spectral characteristics of the Bayer filter, inter-channel cross-talk manifests itself only as signal leakage from the red channel into the remaining channels. The improvement in phase reconstruction quality resulting from the acquisition of an additional hologram frame during a single acquisition, outweighs the detrimental effect of this phenomenon. Both of these constraints come from the use of a single color sensor rather than from the method itself, and could be removed by separating the illumination wavelengths with dichroic mirrors onto individual monochrome cameras – preserving the full SBP of each channel and eliminating color leakage. This comes at the cost of a more complex detection arm and the need for precise registration between the sensors.

The GDRS algorithm employs linear wavelength-dependent phase scaling, which does not account for refractive index dispersion. It should be emphasized, however, that the investigated biological objects are composed primarily of water, which is characterized by minimal absorption in the visible spectral range. Consequently, according to the Kramers–Kronig relations, the change in the refractive index difference within the illumination wavelength range used in this study is negligible, as confirmed by the literature[44,45]. Moreover, dispersion enters solely as a scaling of the retrieved phase values and leaves the reconstructed image itself – its contrast, resolution and the quality of replica separation – entirely unaffected. Importantly, in a wide range of biological applications, the primary objective is to obtain a high-contrast phase image rather than an exact quantitative phase value. Where the dispersion of the sample is known – either from an independent calibration measurement, or, as in the inspection of technical objects, from the material specification itself – the corresponding dispersion coefficient can be directly accounted into the phase scaling, restoring fully quantitative phase reconstruction with no change to the acquisition. Looking further ahead, the spectral diversity on which the method is built carries information about dispersion itself: given a sufficient number of illumination wavelengths, the wavelength dependence of the refractive index could be retrieved jointly with the phase, turning this disadvantage into an additional, spectroscopic contrast mechanism.

In summary, the presented approach constitutes a versatile tool for quantitative phase imaging in common-path shearing configurations. It enables analytical and complete removal of unwanted contributions from replicas, even when imaging dense samples. Transitioning between the two available operating modes - wavelength-scanning and single-shot - requires only changing the camera from monochrome to RGB. Consequently, the method can be applied both to the imaging of static biological samples, enabling detailed representation of their structure (e.g., tissue architecture), and to observing rapidly changing processes in cell cultures, where excellent temporal resolution is crucial. For example, in semen analysis, QPI is frequently used for imaging highly motile cells in dense samples and under non-laboratory conditions[46]. The single-shot mode of the proposed method, implemented in an environmentally robust common-path configuration, enables reliable acquisition of such samples while, owing to the duplicated field of view, allowing simultaneous observation of a larger sample volume. The proposed method therefore represents a promising tool for QPI of a wide range of biomedical applications.

Materials and methods

Experimental setup

In the presented setup, the light source is a partially coherent, tunable laser (supercontinuum laser, NKT Photonics SuperK EVO HP EU-4, equipped with acousto-optic tunable filter SuperK SELECT UV-VIS), enabling sequential wavelength scanning or simultaneous illumination with multiple wavelengths. The beam passes through the sample, the objective (Zeiss 5x/0.12, Nikon 10x/0.25 or Nikon 40x/0.65), the tube lens, and reaches the polarization grating assembly (period of the PG $d = 6.3\ \mu m$).

The polarization state of the generated diffraction orders depends on the polarization of the incident beam. Under linearly polarized illumination, two diffraction orders (±1) are produced with orthogonal circular polarizations (Fig. 1b). In the case of circular polarization, the grating converts it into the orthogonal one[47]. Two identical gratings arranged in series introduce a transverse beam shift τ. Its value depends both on the diffraction angles θ at the two gratings and on the distance z between them. The first grating (PG1) splits the incident beam, transforming its polarization into circular polarization and deflecting the individual diffraction orders at angles $\pm\theta_{\lambda 1}$. According to the grating equation, the diffraction angle θ_λ depends on the wavelength λ and the grating period d. Consequently, the longer the wavelength, the larger the diffraction angle θ_λ and, therefore, the greater the mutual separation of the beams τ_λ. The second grating (PG2) compensates for this deflection; however, the angles $\pm\theta_{\lambda 2}$ at which it diffracts the beam also depend on the mutual rotation angle between the line of the two gratings β. When the gratings are not aligned in parallel ($\beta \neq 0$), the beams propagate relative to each other at an angle ($\theta_{\lambda 1} - \theta_{\lambda 2}$). This phenomenon enables precise control of the fringe spatial frequency in the interferometric image through mutual rotation of the gratings. In the measurements, the introduced carrier frequency had a value typical for the FTM method. The beam separation τ is also influenced by the distance z between the gratings. Reducing this distance shortens the propagation path of the beams at an angle, which leads to a smaller wavefront displacement τ. To enable interference of orthogonally polarized beams, a linear polarizer (LP) is placed in front of the camera. The interference pattern is recorded by a CMOS sensor. To separate the undisturbed phase information from both replicas (orders), it is necessary to record a series of at least $N = 2$ interferograms for different values of τ_λ. This is implemented in two modes: (i) wavelength scanning and (ii) single-shot.

The first mode consists of sequential illumination of the sample with different wavelengths λ and recording interferograms with a monochrome camera (Daheng Mer2-301-125U3M-L, resolution 2048×1536, pixel size 3.45 μm) after each change. The number of interferograms in the series, the spectral range, and the spectral step are selected depending on the requirements. In the second mode, the sample is illuminated simultaneously with discrete wavelengths $\lambda = 458\ nm$, $\lambda = 550\ nm$ and $\lambda = 615\ nm$. A color (RGB) camera (Daheng Mer2-301-125U3C-L, resolution 2048×1536, pixel size 3.45 μm) records a single interferogram, which is separated into three color channels.

As a reference method for changing the replica shear, the approach described in the previous work[41] was used. In this variant, the change in shear value τ results from changing the distance between the gratings. During the experiment, one of the gratings was precisely translated with a step $\delta = 0.5\ mm$ along the optical axis using a motorized linear stage (Thorlabs MTS25/M-Z8). In this way, at a constant illumination wavelength $\lambda = 535\ nm$, a series of $N = 20$ interferograms was recorded using a monochrome camera (Daheng Mer2-301-125U3M-L, resolution 2048×1536, pixel size 3.45 μm).

Data Processing Pipeline and Reconstruction

The reconstruction process is based on a procedure for retrieving and separating overlapping phase images originating from both beam replicas. For this purpose, the GDRS algorithm is employed, representing a new implementation of the MRR[41] method, in which the analytical separation has been replaced with an optimization-based approach, and the entire framework has been extended with a preprocessing stage compensating for dispersion effects. The complete data-processing pipeline is schematically presented in Fig. 2.

The reconstruction process begins with the application of the FTM to each recorded interferogram in order to recover the optical field. Then, using the Angular Spectrum Method (ASM)[42], the field is numerically propagated to the objective focal plane. This step is necessary because the system focus changes with the illumination wavelength, while the sample position remains unchanged during the measurement series, which results in a defocused image for some wavelengths. In addition, changes in wavelength cause variations in magnification, which are corrected through geometric image transformations. In the calibration procedure, the user manually selects characteristic points on the images. Based on the ratio of distances between these points for successive frames, a scaling factor is computed, and the images are then transformed using bicubic interpolation. Once determined, the coefficients for a given wavelength are used for all remaining datasets. The obtained phase maps are also scaled with respect to the wavelength λ, due to the dependence of the phase value on this parameter.

From the optical field prepared in this way for each frame, the phase $\varphi_{\pm 1}$ corresponding to the phase difference between the two interfering replicas, φ_{+1} and φ_{-1}, is retrieved. These values constitute the input data for the main part of the GDRS algorithm. In the first step, based on the sample features, the algorithm determines the displacement $\Delta\mathbf{r}$ (the difference in τ_λ, the difference in τ_λ, where $\mathbf{r} = (x, y)$ and $\Delta\mathbf{r} = (\Delta x, \Delta y)$) between consecutive frames. It then compensates for them separately for negative and positive objects, creating aligned datasets Q_m and Q_p. From these prepared datasets, initial estimates of both objects, U_{m0} and U_{p0}, are determined by searching for the minimum and maximum values, respectively, from the stack of frames for each pixel.

The actual reconstruction proceeds iteratively: the algorithm reconstructs the phase distribution based on the sum of the current estimates of both objects, calculates the error with respect to the input data, and backpropagates its gradient while simultaneously updating both phases. Optionally, background thresholding is applied, limiting the range of reconstructed values. A detailed description of the GDRS algorithm implementation is presented in Supplementary Information.

Sample preparation – neuronal cell cultures

Neuronal cell cultures were prepared as described previously[48,49] with slight modifications. Briefly, rodent brains were removed into dissociation medium (DM; 81.8 mM Na_2SO_4, 30 mM K_2SO_4, 5.8 mM $MgCl_2$, 0.25 mM $CaCl_2$, 1 mM HEPES, pH 7.4, 20 mM glucose, 1 mM kynurenic acid, and 0.001% phenol red). Brain tissue chunks were next incubated in papain solution (100 U in DM) for 15 min at 37 °C and washed three times with DM. The tissue was subsequently rinsed three times in plating medium (PM; Minimum Essential Medium supplemented with 10% fetal bovine serum and 1% penicillin–streptomycin) and gently triturated to obtain a single-cell suspension. Cells were diluted, centrifuged and resuspended in PM and plated on coated coverslips. After 2 h, the plating medium was replaced with maintenance medium (MM; Neurobasal-A supplemented with 2% B-27 and 1% penicillin–streptomycin). For the experiment we used cell cultures of approximately 14 DIV. The cells were briefly rinsed in PBS, fixed for 15 minutes in 4% paraformaldehyde and mounted onto glass slide.

Sample preparation – yeast

Food-grade Saccharomyces cerevisiae yeast was prepared by suspending c.a. 0.5 g of yeast in 10 mL of warm water supplemented with 0.5 g of sugar (sucrose). The suspension was gently mixed and incubated for 10 min. Subsequently, 40 μL of the suspension was applied onto a microscope slide and covered with a coverslip.

Code availability

The algorithm used in this study is provided as part of the Supplementary Information.

Data availability

The raw data supporting the findings of this study are available from the corresponding author upon reasonable request.

Supplementary information accompanies the manuscript on the Light: Science & Applications website (http://www.nature.com/lsa).

References

1 Popescu G. Quantitative Phase Imaging of Cells and Tissues. *McGraw-Hill Educ* 2011.

2 Park Y, Depeursinge C, Popescu G. Quantitative phase imaging in biomedicine. *Nat Photonics* 2018; **12**: 578–589.

3 Barer R. Determination of Dry Mass, Thickness, Solid and Water Concentration in Living Cells. *Nature* 1953; **172**: 1097–1098.

4 Wang Z, Millet L, Chan V, Ding H, Gillette MU, Bashir R *et al.* Label-free intracellular transport measured by spatial light interference microscopy. *J Biomed Opt* 2011; **16**: 026019.

5 Ma L, Rajshekhar G, Wang R, Bhaduri B, Sridharan S, Mir M *et al.* Phase correlation imaging of unlabeled cell dynamics. *Sci Rep* 2016; **6**: 32702.

6 Huang D, Leslie KA, Guest D, Yeshcheulova O, Roy IJ, Piva M *et al.* High-Speed Live-Cell Interferometry: A New Method for Quantifying Tumor Drug Resistance and Heterogeneity. *Anal Chem* 2018; **90**: 3299–3306.

7 Polanco ER, Moustafa TE, Butterfield A, Scherer SD, Cortes-Sanchez E, Bodily T *et al.* Multiparametric quantitative phase imaging for real-time, single cell, drug screening in breast cancer. *Commun Biol* 2022; **5**: 794.

8 Wang Z, Tangella K, Balla A, Popescu G. Tissue refractive index as marker of disease. *J Biomed Opt* 2011; **16**: 116017.

9 Wyant JC. White Light Extended Source Shearing Interferometer. *Appl Opt* 1974; **13**: 200–202.

10 Patorski K. Conjugate lateral shear interferometry and its implementation. *JOSA A* 1986; **3**: 1862–1870.

11 Anand A, Chhaniwal V, Javidi B. Tutorial: Common path self-referencing digital holographic microscopy. *APL Photonics* 2018; **3**: 071101.

12 Zhang J, Dai S, Ma C, Xi T, Di J, Zhao J. A review of common-path off-axis digital holography: towards high stable optical instrument manufacturing. *Light Adv Manuf* 2021; **2**: 333–349.

13 Zdańkowski P, Winnik J, Patorski K, Gocłowski P, Ziemczonok M, Józwik M *et al.* Common-path intrinsically achromatic optical diffraction tomography. *Biomed Opt Express* 2021; **12**: 4219–4234.

14 Bhaduri B, Edwards C, Pham H, Zhou R, Nguyen TH, Goddard LL *et al.* Diffraction phase microscopy: principles and applications in materials and life sciences. *Adv Opt Photonics* 2014; **6**: 57–119.

15 Velghe S, Primot J, Guérineau N, Cohen M, Wattellier B. Wave-front reconstruction from multidirectional phase derivatives generated by multilateral shearing interferometers. *Opt Lett* 2005; **30**: 245–247.

16 Popescu G, Ikeda T, Dasari RR, Feld MS. Diffraction phase microscopy for quantifying cell structure and dynamics. *Opt Lett* 2006; **31**: 775–777.

17 Bon P, Maucort G, Wattellier B, Monneret S. Quadriwave lateral shearing interferometry for quantitative phase microscopy of living cells. *Opt Express* 2009; **17**: 13080–13094.

18 Hillman TR, Lue N, Sung Y, Dasari RR, Yaqoob Z. Near-Common-Path Self-Reference Quantitative Phase Microscopy. *IEEE Photonics Technol Lett* 2012; **24**: 1812–1814.

19 Mico V, Ferreira C, Zalevsky Z, García J. Spatially-multiplexed interferometric microscopy (SMIM): converting a standard microscope into a holographic one. *Opt Express* 2014; **22**: 14929–14943.

20 Trusiak M, Picazo-Bueno J-A, Patorski K, Zdańkowski P, Mico V. Single-shot two-frame π-shifted spatially multiplexed interference phase microscopy. *J Biomed Opt* 2019; **24**: 1–8.

21 Patorski K, Zdańkowski P, Trusiak M. Grating deployed total-shear 3-beam interference microscopy with reduced temporal coherence. *Opt Express* 2020; **28**: 6893–6908.

22 Guo R, Mirsky SK, Barnea I, Dudaie M, Shaked NT. Quantitative phase imaging by wide-field interferometry with variable shearing distance uncoupled from the off-axis angle. *Opt Express* 2020; **28**: 5617–5628.

23 Lee K, Park Y. Quantitative phase imaging unit. *Opt Lett* 2014; **39**: 3630–3633.

24 Baek Y, Lee K, Yoon J, Kim K, Park Y. White-light quantitative phase imaging unit. *Opt Express* 2016; **24**: 9308–9315.

25 Běhal J, Ježek M. Incoherent lateral shearing digital holographic microscopy. *Optica* 2025; **12**: 620–625.

26 Ghim Y-S, Rhee H-G, Davies A, Yang H-S, Lee Y-W. 3D surface mapping of freeform optics using wavelength scanning lateral shearing interferometry. *Opt Express* 2014; **22**: 5098–5105.

27 Shanmugam P, Light A, Turley A, Falaggis K. Variable shearing holography with applications to phase imaging and metrology. *Light Adv Manuf* 2022; **3**: 193–210.

28 Yatagai T, Kanou T. Aspherical Surface Testing with Shearing Interferometer Using Fringe Scanning Detection Method. *Opt Eng* 1984; **23**: 357–360.

29 Tian X, Itoh M, Yatagai T. Simple algorithm for large-grid phase reconstruction of lateral-shearing interferometry. *Appl Opt* 1995; **34**: 7213–7220.

30 Okuda S, Nomura T, Kamiya K, Miyashiro H, Yoshikawa K, Tashiro H. High-precision analysis of a lateral shearing interferogram by use of the integration method and polynomials. *Appl Opt* 2000; **39**: 5179–5186.

31 Winnik J, Suski D, Heto M, Lenarcik M, Ziemczonok M, Kołodziejczyk M *et al*. OSI-flex: optimization-based shearing interferometry for joint phase and shear estimation using a flexible open-source framework. *J Phys Photonics* 2026; **8**: 015036.

32 Tayal S, Usmani K, Singh V, Dubey V, Singh Mehta D. Speckle-free quantitative phase and amplitude imaging using common-path lateral shearing interference microscope with pseudo-thermal light source illumination. *Optik* 2019; **180**: 991–996.

33 Tang X, Cao Z, Wang Z, Xie H, Xu L. Retrieval of Phase and Temperature Distributions in Axisymmetric Flames From Phase-Modulated Large Lateral Shearing Interferogram. *IEEE Trans Instrum Meas* 2021; **70**: 1–12.

34 Zdańkowski P, Winnik J, Rogalski M, Marzejon MJ, Wdowiak E, Dudka W *et al*. Polarization Gratings Aided Common-Path Hilbert Holotomography for Label-Free Lipid Droplets Content Assay. *Laser Photonics Rev* 2025; **19**: 2401474.

35 Girshovitz P, Shaked NT. Doubling the field of view in off-axis low-coherence interferometric imaging. *Light Sci Appl* 2014; **3**: e151–e151.

36 Edwards C, Zhou R, Hwang S-W, McKeown SJ, Wang K, Bhaduri B *et al*. Diffraction phase microscopy: monitoring nanoscale dynamics in materials science [Invited]. *Appl Opt* 2014; **53**: G33–G43.

37 Tang Z, Winnik J, Hennelly BM. Optical diffraction tomography using a self-reference module. *Biomed Opt Express* 2025; **16**: 57–67.

38 Rubio-Oliver R, Micó V, Zalevsky Z, García J, Angel Picazo-Bueno J. Quantitative phase imaging by automated Cepstrum-based interferometric microscopy (CIM). *Opt Laser Technol* 2024; **177**: 111121.

39 Rubio-Oliver R, García J, Zalevsky Z, Picazo-Bueno JÁ, Micó V. Cepstrum-based interferometric microscopy (CIM) for quantitative phase imaging. *Opt Laser Technol* 2024; **174**: 110626.

40 Rubio-Oliver R, Micó V, García J, Picazo-Bueno JÁ. Cepstrum-based interferometric microscopy with rolling-shutter cameras. *Opt Lett* 2025; **50**: 2465–2468.

41 Rogalski M, Zdańkowski P, Heto M, Mierzejewska J, Lenarcik M, Li Z *et al*. Doubling the field of view and eliminating the replica overlap problem in common-path shearing quantitative phase imaging. *J Phys Photonics* 2025; **8**: 015018.

42 Matsushima K, Shimobaba T. Band-Limited Angular Spectrum Method for Numerical Simulation of Free-Space Propagation in Far and Near Fields. *Opt Express* 2009; **17**: 19662–19673.

43 Kronig R de L. On the Theory of Dispersion of X-Rays. *JOSA* 1926; **12**: 547–557.

44 Marcuse D. *Light Transmission Optics*. Van Nostrand Reinhold, 1982.

45 Zuo C, Li J, Sun J, Fan Y, Zhang J, Lu L *et al*. Transport of intensity equation: a tutorial. *Opt Lasers Eng* 2020; **135**: 106187.

46 Lee W, Choi J-H, Ryu S, Jung D, Song J, Lee J-S *et al*. Color-coded LED microscopy for quantitative phase imaging: Implementation and application to sperm motility analysis. *Methods* 2018; **136**: 66–74.

47 Blain P, Piron P, Renotte Y, Habraken S. An in-line shearography setup based on circular polarization gratings. *Opt Lasers Eng* 2013; **51**: 1053–1059.

48 Winnik J, Zdańkowski P, Stefaniuk M, Ahmad A, Zuo C, Ahluwalia BS *et al*. Gradient optical diffraction tomography. *Commun Phys* 2025; **8**: 510.

49 Stefaniuk M, Swiech L, Dzwonek J, Lukasiuk K. Expression of Ttyh1, a member of the Tweety family in neurons in vitro and in vivo and its potential role in brain pathology. *J Neurochem* 2010; **115**: 1183–1194.

Acknowledgements

This work was funded by the National Science Center Poland (2024/55/D/ST7/02792). The study was conducted on devices co-funded by the Warsaw University of Technology within the Excellence Initiative: Research University (IDUB) program. Research was partially financed by the Project No. WPC3/2022/47/INTENCITY/2024 funded by the National Centre for Research and Development (NCBR) under the 3rd Polish-Chinese/Chinese-Polish Joint Research Call (2022). MS was supported by the BRAINCITY project (FENG.02.01-IP.05-0010/24). BRAINCITY is carried out within the International Research Agenda Programme of the Foundation for Polish Science, co-financed by the European Union under the European Regional Development Fund.

Author Contributions

A.P.: Investigation, Visualization, Writing – original draft. M.R.: Methodology, Software, Data curation, Formal analysis, Validation, Writing – review & editing. M.S.: Resources. M.T.: Supervision, Conceptualization, Resources, Writing – review & editing. P.Z: Methodology, Supervision, Conceptualization, Resources, Funding acquisition, Writing – original draft, Writing – review & editing.

Conflict of Interest

The authors declare no competing interests.

Supplementary Information

Supplementary Information for this paper is available in Supplementary Document 1. It includes Supplementary Notes 1-2 and Supplementary Figures S1–S2

Supplementary Files

This is a list of supplementary files associated with this preprint. Click to download.

- DrozdzeMRlapazpfiltered.mp4
- SISingleShotReplicaFreeQPILSA.pdf